Available online at www.sciencedirect.com
SCIENCE DIRECT®
Journal of Solid State Chemistry 177 (2004) 109–118
JOURNAL OF SOLID STATE CHEMISTRY
http://elsevier.com/locate/jssc

Lithium insertion into In_2S_3 studied by perturbed γ–γ angular correlation

A. Kulińska,[a,b] M. Uhrmacher,[a,*] R. Dedryvère,[a,c] A. Lohstroh,[a] H. Hofsäss,[a] K.P. Lieb,[a] A. Picard-Garcia,[c] and J.-C. Jumas[c]

[a] *II. Physikalisches Institut, Universität Göttingen, Tammannstrasse 1, D-37077, Göttingen, Germany*
[b] *The Henryk Niewodniczański Institute of Nuclear Physics, ul. Radzikowskiego 152, Pl-31-342 Kraków, Poland*
[c] *Laboratoire des Agrégats Moléculaires et des Matériaux Inorganiques (UMR 5072 CNRS), CC15, Université Montpellier 2, F-34095 Montpellier cédex 5, France*

Received 14 January 2003; received in revised form 21 May 2003; accepted 2 June 2003

Abstract

$Li_xIn_2S_3$ was electrochemically prepared with different small amounts x of lithium ($0 \leqslant x \leqslant 0.13$) in order to maintain the initial crystallographic structure of the thiospinel In_2S_3. About 10^{12} radioactive ^{111}In ions have been implanted into these samples at 400 keV to perform PAC experiments in the temperature range from 10 to 773 K. The results are compared to previous experiments with undoped In_2S_3 samples. According to the structure of In_2S_3 in the β-phase, which belongs to the $I4_1/amd$ space group having a unit cell with 32 In and 48 S atoms and the cell parameters $\alpha = 7.61$ Å and $c = 32.28$ Å, three different electric field gradients were observed. Within two different temperature ranges dynamical EFGs occur, which are clearly influenced by the insertion of Lithium. The strong dependence of one EFG on the Li concentration x can be correlated to the effective charge of the In ions. This correlation is discussed with respect to XRD analyses of the $Li_xIn_2S_3$ samples and to XANES measurements on a similar sample.

Keywords: Li intercalation; Thiospinel; Lattice location; Dynamical EFG; Perturbed angular correlation (PAC); XANES

1. Introduction

Among the rechargeable electrochemical generators, the lithium batteries deliver the highest voltage (3.6–3.9 V) and offer the highest storable energy per volume and weight [1]. To avoid safety problems due to the Li anode in the Li-metal battery, the concept of Li-ion battery was proposed [2] and Li-ion batteries are now considered as the best systems for powering portable electronic devices, such as cellular phones or lap-top computers [3]. In the Li-ion battery, both anode and cathode consist of intercalated materials. Despite the commercial success of the typical system using a lithium cobaltate ($LiCoO_2$) cathode, a carbonaceous anode (graphite or coke) and a liquid electrolyte, an important research is being carried out to improve the performance of the three battery components. Concerning the anode materials, the main research efforts are aimed at alloys [4], metal oxides [5,6] and nitrides [7].

Sulfide compounds of transition metals (Cu, Co, Fe) and post-transition metals (In, Sn) with a spinel-related structure have shown an interesting behavior as host materials for lithium insertion, and compounds such as $FeIn_2S_4$, $In_2Sn_{0.5}S_4$, $CuCo_{0.5}Sn_{1.5}S_4$ or $CuInSnS_4$ [8–11] have been revealed as possible anode materials for lithium-ion batteries, provided the reversibility of the lithium insertion in these materials can be improved. All these compounds are solid solutions based on the defect spinel structure of indium sulfide (In_2S_3).

In the present study we applied the perturbed angular correlation (PAC) method to investigate In_2S_3, the simplest thiospinel of this family of compounds, in order to better understand the mechanisms that occur during Li insertion. PAC-experiments measure the hyperfine interaction between a radioactive probe and the electric field gradient (EFG) generated by the direct neighborhood at the site of the probe atom. In our experiments we used the probe ^{111}In which decays via

*Corresponding author. Fax: +49-551-394-493.
E-mail address: muhrmac@gwdg.de (M. Uhrmacher).

0022-4596/$ - see front matter © 2003 Published by Elsevier Inc.
doi:10.1016/S0022-4596(03)00328-1

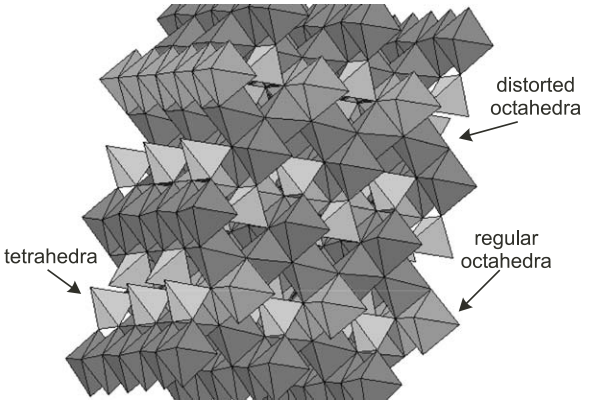

Fig. 1. Crystalline structure of β-In_2S_3 compound. The three different sulfur polyhedra are differently shaded. Each one contains one In ion.

electron capture (EC) to ^{111}Cd. Intercalation of Li into the In_2S_3 lattice should result in observable changes of the position and/or charge of the host atoms which determine the EFG. Furthermore, the ^{111}In probe is not a foreign atom in this compound and will thus occupy regular In lattice sites.

The so-called "normal spinel" is characterized by the equation $(A^{2+})[B_2^{3+}]X_4^{2-}$, where the A^{2+}-cations are found in the X-tetrahedra and the B^{3+}-cations in the X-octahedra. The good properties of spinel compounds as host materials for lithium insertion can be explained by the presence of empty tetrahedrally and octahedrally coordinated sites in the structure [12]. By comparison, In_2S_3 is cation-deficient and offers an additional number of empty tetrahedral sites: $(A^{2+}_{0.67}\mathrm{vac}_{0.33})[B_2^{3+}]X_4^{2-}$. It is thus an ideal candidate for storing large amounts of Li within the lattice and applying the PAC-technique with ^{111}In probes to investigate the local changes caused by the Li insertion. At room temperature, In_2S_3 occurs in the β-phase, which is a cation-ordered tetragonal structure belonging to the $I4_1/amd$ space group. The unit cell contains 32 In and 48 S atoms and has the cell parameters $a = 7.61$ Å and $c = 32.28$ Å [13]. It is composed of octahedra and tetrahedra, as shown in Fig. 1. Eight In atoms are in the center of regular sulfur-octahedra (position 8(c)), another 16 are in the center of sulfur octahedra with slightly distorted symmetry—visible as the zigzag of its baseline (position 16(h)). The remaining eight In atoms are placed in the center of sulfur tetrahedra (position 8(e)).

2. Experimental

2.1. Sample preparation and characterization

In_2S_3 samples were synthesized from the elements by a solid state reaction. Indium and sulfur (3% excess) were mixed and sealed in silica tubes under vacuum at $\sim 10^{-3}$ Pa. The mixture was slowly heated at 1°C/min to 673 K and held at this temperature for 10 h, then kept at 1023 K for 10 h, and finally at 1123 K for 5 days. The samples were then slowly cooled down to room temperature.

Electrochemical lithium insertion was carried out in Swagelok^{TM} test cells, using In_2S_3 as the positive electrode and Li metal as the negative electrode, both separated by a glass fiber separator soaked in a 1 M $LiPF_6$ in EC:DMC (1:1 mixture of ethylene carbonate and dimethyl carbonate) electrolyte solution. The positive electrode was prepared by pressing 10 mg of pure In_2S_3 powder at about 4 tons/cm^2 over a 7 mm stainless steel grid. Electrochemical Li insertions were carried out by means of a "Mac Pile" system (BioLogic, France), operating in galvanostatic mode with a current of 5 μA (corresponding to a current density of 13 μA/cm^2). $Li_xIn_2S_3$ samples with lithium concentrations of up to $x = 0.16$ Li/mol were obtained with an uncertainty of $\sim 5\%$.

X-ray powder diffraction (XRD) characterization was performed with a Bruker D8 $\theta-2\theta$ diffractometer using Cu$K\alpha$ radiation and a LiF monochromator. Rietveld refinements of the XRD patterns of pristine and lithiated samples were carried out with the program FullProf2000 [14]. The XRD analysis confirmed the tetragonal structure of the β-In_2S_3 phase with space group $I4_1/amd$.

Radioactive $^{111}In^+$ ion implantations, necessary for PAC experiments, were carried out with the Göttingen ion-implanter IONAS [15,16]. About 10^{12} $^{111}In^+$ ions were implanted at 100 or 400 keV into the inserted electrodes, leading to depth distributions peaking below 100 nm. After the implantation, the supporting stainless steel grid was removed to exclude any disturbance of the PAC spectra by ^{111}In probes which might have been implanted into the grid. The radiation damage caused by the implantation was removed by a 723 K 1 h annealing in vacuum. The annealed samples were cooled down to room temperature within 2 h or measured directly after annealing at elevated temperatures.

X-ray absorption near edge spectroscopy (XANES) measurements were carried out at LURE (Orsay, France). The SK-edge spectra were recorded at the Super ACO storage ring in the total electron yield mode, by measuring the photocurrent from the insulated metallic sample holder with a pico-amperemeter. The powder samples were inlayed on indium foils to maximize electrical conduction. Two parallel Si(111) crystals were used as monochromators for the sulfur K-edge, allowing a resolution of 0.3 eV. The indium L_I edge spectra were recorded at DCI storage ring in transmission mode. Two parallel Si(311) crystals were used as monochromators, allowing a resolution of 0.2 eV. The samples were placed between two ion chambers which were used to measure the incident (I_0)

and transmitted (I) intensities. The samples were prepared by depositing the finely ground, polycrystalline powders, sieved to 5 μm, onto the membrane filters.

2.2. Perturbed $\gamma-\gamma$ angular correlation technique

The PAC method is one of the nuclear solid state methods appropriate for studying the structural and electronic properties of probe atoms in solids. It measures the hyperfine interaction, supplying information about the local electric and chemical environment of the probe atoms. A detailed description of this method can be found in Refs. [17,18]. Here we will shortly present how the electric field gradient (EFG) acting on the probe nuclei in a compound can be determined.

The electric quadrupole interaction is caused by the interaction of the nuclear quadrupole moment Q of the probe nucleus with the EFG tensor V_{ij} acting at this site, defined as the second partial derivative of the electric potential $\Phi(\vec{r})$. The V_{ij} tensor is defined to be traceless within the principal axis system; it is chosen in such a way that one gets $|V_{xx}| \leqslant |V_{yy}| \leqslant |V_{zz}|$. Therefore, in most cases the EFG can be characterized by just two parameters: the asymmetry parameter $\eta = (V_{xx}-V_{yy})/V_{zz}$, which represents the deviation from the axial symmetry ($0 \leqslant \eta \leqslant 1$), and V_{zz} the largest EFG component in the principal axis system, which represents the strength of the EFG.

In our experiments the isotope ^{111}In was used as the probe atom. With a half-life of $T_{1/2} = 2.83$ days it decays by electron capture (EC) to the excited $7/2^+$ state of ^{111}Cd, which in turn decays to the $1/2^+$ ground state of ^{111}Cd by emitting a 171–245 keV γ–γ cascade. The intermediate isomeric $5/2^+$ level has a half-life of $T_{1/2} = 85$ ns and is characterized by the quadrupole moment $Q = 0.83(13)$ b and the magnetic moment $\mu = -0.7656(25)\ \mu_n$ [18]. The hyperfine interaction of the quadrupole moment Q of the isomeric $5/2^+$ state with an EFG results in the hyperfine splitting of that level into three sublevels. The transition energies between these levels are proportional to the quadrupole frequency ω_Q, described by

$$\omega_Q = \frac{eQV_{zz}}{4I(2I-1)\hbar}. \tag{1}$$

Usually, a derived quantity is used–the quadrupole coupling constant ν_Q, which is independent of the nuclear spin I.

$$\nu_Q = \frac{eQV_{zz}}{h}. \tag{2}$$

Since the quadrupole frequency is proportional to the largest component V_{zz}, it gives information about the EFG strength acting at the lattice site of the probe atom.

The basic requirement of PAC is an anisotropic angular correlation of the two γ-rays of the cascade. Detection of γ_1 in a certain direction will lead to a preferential emission direction of γ_2, relative to the direction of γ_1 The probability distribution of finding γ_2 at the angle θ and the time t with respect to the direction and emission time $t_1 = 0$ of γ_1 in polycrystalline material is expressed as

$$W(\theta, t) = 1 + A_{22}G_{22}(t)P_2(\cos\theta). \tag{3}$$

A_{22} is the anisotropy coefficient of the $\gamma\gamma$ cascade, $P_2(\cos\theta)$ is the second Legendre polynomial, and $G_{22}(t)$ is the perturbation factor containing all the information on the hyperfine interaction. The formula for the perturbation factor $G_{22}(t)$ can be obtained in lowest order as

$$G_{22}(t) = \sum_{n=0}^{3} s_{2n}(\eta)\cos(\omega_n t) \times \exp[-g_{2n}(\eta)\delta t] \times d\left[-g_{2n}(\eta)\nu_Q t, \tau_R\right]. \tag{4}$$

The parameters $\omega_n = g_n(\eta)\nu_Q$ are the primary transition frequencies and s_{2n} denotes their amplitudes. $g_n(\eta)$ describes the quadrupole splitting of the intermediate state of the probe nucleus, caused by the EFG. The values of the s_{2n} and $g_n(\eta)$ for the applied ^{111}Cd probe are tabulated in Ref. [19]. Due to the finite time resolution τ_R of the apparatus an additional damping of the oscillation amplitudes occurs, which is parameterized by the function $d[-g_{2n}(\eta)\nu_Q t, \tau_R]$.

Experimental PAC spectra in more complex situations show, in addition to the instrumental damping, different deviations from Eq. (4). In most cases, this damping arises from the occurrence of similar static EFGs which are caused by small distortions in the neighborhood of the probe atom. This broadening of the EFG is described by the width δ of a Lorentzian or a Gaussian distribution. Another damping mechanism arises if the hyperfine environment of the probe nucleus changes during the lifetime of the sensitive level: this dynamic hyperfine interaction (HFI) causes $G_{22}(t) \to 0$, in contrast to the case of a static HFI where the G_{22} factor reaches the so-called "hard-core value" which is equal to the s_{20} value. For this special type of dynamic hyperfine interaction, the experimental PAC spectra can be fitted with an exponential function $R(t) \propto \exp(-\lambda t)$.

The PAC measurements were carried out in a conventional slow–fast set-up of four NaI detectors in 90° geometry having a time resolution of $\tau_R = 3.5$ ns for the 171–245 keV cascade in ^{111}Cd. The twelve $\gamma\gamma$ coincidence spectra $N(\theta, t)$ obtained from all possible combinations of the detectors were used to generate the experimental perturbation function.

$$R(t) = 2\frac{N(180^\circ, t) - N(90^\circ, t)}{N(180^\circ, t) + 2N(90^\circ, t)}. \tag{5}$$

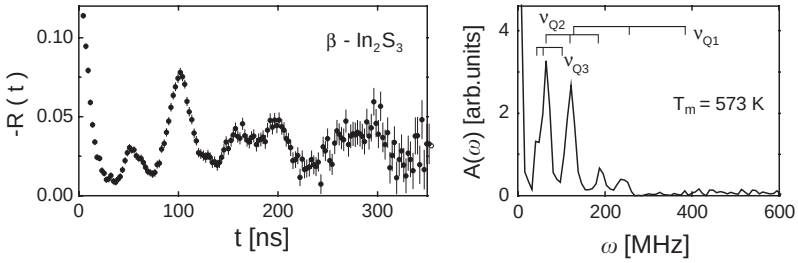

Fig. 2. PAC spectrum taken for ^{111}Cd in β-In_2S_3 (left) and its Fourier transform (right). Indicated are the triplets of ω_n corresponding to the quadrupole coupling constants ν_{Qn}.

In the case of several purely static hyperfine interaction the experimental $R(t)$ spectrum can be fitted with the expression

$$R(t) = A_{22} \sum_{i=1}^{k} f_i G_{22}^i(t). \quad (6)$$

The sum runs over all the different lattice environments i of the probes. In such a case the various observed fractions f_i indicate the population of non-equivalent probe sites in the sample which are characterized by their different EFG parameters. The Fourier transform exhibits one triplet of ω_n values for each non-equivalent probe site, described by the quadrupole coupling constant ν_{Qi} and the asymmetry parameter η_i. We used the CERN program code MINUIT to fit the data. In principle, five different probe sites can be fitted simultaneously, each one characterized by the four parameters ν_{Qi}, η_i, δ_i and f_i. Nevertheless, the existence of already three different EFGs with some overlapping Fourier components requires a certain strategy in fitting the data, as will be explained later. Fig. 2 presents a typical experimental PAC spectrum and the corresponding Fourier transform taken for ^{111}Cd probes in a pure β-In_2S_3 sample. The triplets of the primary transition frequencies $\omega_{ni} (n = 1, 2, 3)$, attributed to the three different EFGs $(i = 1, 2, 3)$ observed in this sample, are marked.

3. Experimental results

3.1. PAC measurements in pure In_2S_3

The PAC probe ^{111}In is chemically identical with one of the components of In_2S_3 and will therefore occupy all the possible non-equivalent substitutional sites. Detailed measurements in the pure β-In_2S_3 phase were performed by Aldon et al. [20]. These authors identified three different sites of ^{111}In, one tetrahedral (8(e)) site and the two non-equivalent octahedral ones (8(c) and 16(h)), in agreement with the crystallographic data (see Fig. 1). Fig. 3 shows the PAC patterns with their corresponding Fourier transforms taken at room temperature, 473 and 728 K for a polycrystalline In_2S_3 sample.

The data shown in Fig. 3c were recorded at $T_m = 728$ K, i.e., above the temperature ($T = 693$ K), where the phase transition from β-In_2S_3 to the cubic α-In_2S_3 phase takes place. In the α-phase we find the same octahedral and tetrahedral building blocks of the crystalline structure as in the β-phase, but in the α-phase the vacant tetrahedra are randomly distributed, whereas they are ordered in the β-phase. This phase transition was investigated in detail with the PAC-technique [21]. It was found (cf. also Fig. 3c) that in the α-phase a dynamic behavior of the hyperfine interaction occurs, visible as $R(t) \sim G_{22}(t) \to 0$ for $t > 50$ ns. Typically, the high temperature spectrum of the α-phase can be described by a very broad ($\sim$420 MHz) frequency distribution around $\nu_Q = 0$ or by an exponential function $\exp(-\lambda t)$ with a decay constant of $\lambda \sim 83$ MHz.

As already mentioned in the previous chapter, a dynamic HFI arises when the direct neighborhood of the probes changes during the PAC observation time (within about 200 ns). Searching for the physical reason of this fast change we have to state that in the α-phase *the In atoms on tetrahedral sites leave their sites*. This agrees well with the crystallographic information that the tetrahedral sites change their occupancy from regular to random during the $\beta \to \alpha$ transition. The high mobility of the tetrahedrally coordinated In atoms is a direct consequence of the large number of vacant sites in this structure. Indeed, each occupied tetrahedral site 8(e) shares a face with four vacant octahedral sites, while each vacant octahedral site shares a face with two vacant tetrahedral sites, furthermore, each vacant tetrahedral site also shares a face with four vacant octahedral sites. Hence it is very easy for In ions to jump in all directions from a tetrahedral site to vacancies. On the other hand, In atoms on octahedral sites have no structurally available vacancies as next neighbors and they seem to remain on their sites. Here we want to point out the fact that in Li-free samples In ions are mobile in the α-phase, which is the clue to understand which ion species is the mobile one.

Fig. 3a shows a second type of damping behavior of these PAC spectra obtained in *pure* β-In_2S_3 at room

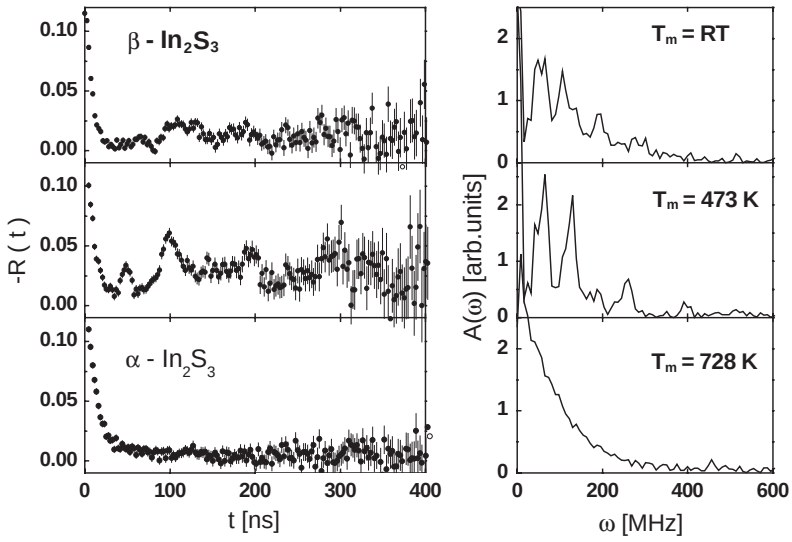

Fig. 3. PAC spectra and the corresponding Fourier transform for ^{111}Cd probes in pure In_2S_3 taken at the indicated measuring temperatures T_m.

temperature, which disappears at lower ($T_m \leqslant 150$ K) and higher ($T_m \geqslant 350$ K) temperatures. It was explained in detail as being due to the "after-effect" of the ^{111}In electron capture [21], similar as for ^{111}In in the oxides La_2O_3 [22] and In_2O_3 [23]. Again, the origin of the dynamic HFI, which leads to the damping of the PAC spectrum, is a change in the next neighborhood of a probe within the observation time. The probe nucleus ^{111}In decays via electron capture (EC) to an excited nuclear state of ^{111}Cd. This violent decrease of the proton number Z completely changes its electronic system, which gets highly excited and charged via Auger-transitions. De-excitation then proceeds within fs—provided enough mobile electrons are available, as in metals. However, in many semiconductors and insulators the de-excitation proceeds on much longer time scales, and the "after-effect" is observed in the PAC spectra measured with ^{111}In [24,25]. One way of influencing the after-effect is to dope the material with an electron donor (like in La_2O_3 [22]), which also leads to un-damped spectra. Lithium is an electron donor in β-In_2S_3 and, in fact, it has been shown that in Li-doped samples the after-effect damping disappears at all temperatures [21].

At higher temperatures ($T_m = 473$ K, Fig. 3b) and ($T_m = 573$ K, Fig. 2) the PAC spectra of *pure* β-In_2S_3, are less obscured by dynamic damping. These spectra were fitted with a set of three quadrupole interactions: $\nu_Q(8c) = 137.8(11)$ MHz, $\eta_{8c} = 0.04(1)$; $\nu_Q(16\,h) = 63.4(9)$ MHz, $\eta_{16h} = 0.19(1)$; and $\nu_Q(8e) = 35(1)$ MHz, $\eta_{8e} = 0.52(1)$. The ratio of the fractions f_{8c}:f_{16h}: $f_{8e} \approx 1{:}2{:}1$ corresponds very well with the relative populations of the 8(c), 16(h) and 8(e) sites, as expected from the crystallographic data. Although PAC measurements with ^{111}In probes in *pure* In_2S_3 are complicated by the two different types of dynamic behavior, their results are understood in detail [21] and can be used to demonstrate the effects of Li doping as will be shown in the next section.

3.2. PAC measurements in Li-doped In_2S_3 samples

As described in Section 2.1, $Li_xIn_2S_3$ was electrochemically prepared with different amounts x of lithium. Small lithium contents were chosen for our experiments ($0 \leqslant x \leqslant 0.13$) in order to maintain the initial crystallographic structure of In_2S_3. Nevertheless, a lithium content $x = 0.125$ means that every second empty tetrahedron may contain one inserted Li atom. Compared to the 10^{12} implanted radioactive ^{111}In ions or the usual doping with donor atoms, this number of inserted Li atoms is huge. The PAC experiments were done in the temperature range from 10 to 773 K. PAC spectra in $Li_xIn_2S_3$ samples taken at 473 K for different values of x are presented in Fig. 4. At this temperature, where the "after-effect damping" has only a small effect on pure In_2S_3, one can observe additional damping effects in Li-doped samples. In fact, the insertion of lithium causes two different types of changes in the PAC spectra: the first one is the appearance of an additional *dynamic fraction* f_d in parallel with a lowering of the tetrahedral fraction f_{8e}. The second one is a temperature and concentration dependence of the strength of (at least) one EFG.

With an increasing Li concentration of $x \geqslant 0.05$ Li/mol, the damping of the PAC pattern increases drastically (see Fig. 4). A similar behavior was found when a sample with a fixed Li content x was measured at different temperatures. The Fourier transforms from samples with a higher x look similar to a mixture of an

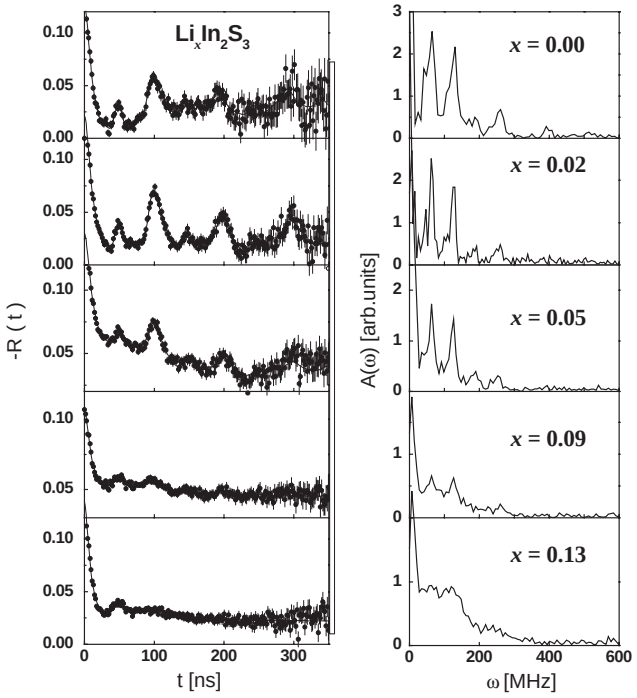

Fig. 4. PAC patterns and Fourier transforms taken at $T_m = 473$ K for ^{111}Cd in $Li_xIn_2S_3$ for different Li contents x.

"α-phase background" and of pure β-In_2S_3. In order to model this behavior, we fitted the experimental data with the three EFGs corresponding to the three indium sites in the $Li_xIn_2S_3$ lattice (see Section 3.1.) and an additional dynamic fraction ($f_d \propto \exp(-\lambda t)$). In fact, only such a "four-fraction assumption" gave a reasonable fit. At low x-values a fit with only three fractions and a slightly enlarged δ-parameter can describe the data, too. To obtain a consistent fitting procedure we applied the four-fraction assumption to all Li-doped samples. In the case of $Li_{0.02}In_2S_3$ (measured at 473 K), the additional dynamic fraction f_d reached about 20% and the three In lattice sites were characterized by the PAC parameters known from undoped In_2S_3. While fitting the data collected at different temperatures and Li contents, some fractions of the different sites and their characteristic PAC parameters, as well, turned out to be temperature dependent.

The temperature evolution of the dynamic fraction f_d for different lithium contents x in $Li_xIn_2S_3$ is presented in Fig. 5. Even at low temperatures, dynamic behavior of the perturbation function can be observed: for the sample with $x = 0.02$, about 25% of the probes experience a dynamic HFI at $T_m = 10$ K. With increasing temperature the fraction f_d increases slightly for all Li concentrations ($f_d = 58\%$ for $x = 0.05$), but no sharp $\beta \rightarrow \alpha$ phase transition at 683 K was observed, as in the case of pure In_2S_3 [26]. In Fig. 6 all available values of the dynamic fraction f_d, taken at three different temperatures, are plotted versus the Li content x. The

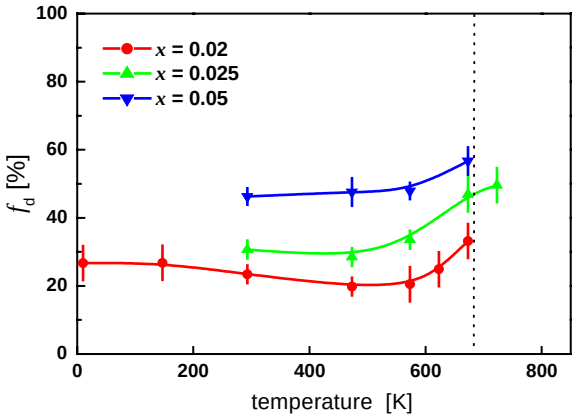

Fig. 5. The temperature dependence of the dynamic fraction f_d for increasing lithium content. The dashed line marks the temperature of the $\beta \rightarrow \alpha$ phase transition.

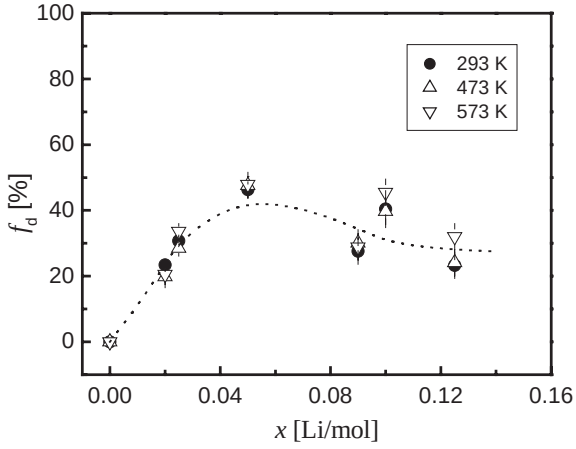

Fig. 6. The change of the dynamic fraction f_d with the Li content x in $Li_xIn_2S_3$.

general trend seems to be independent of the measuring temperature. It has a maximum near $x = 0.05$.

In the case of pure In_2S_3 [20], the populations of the three well-defined In lattice sites follow well the expected values $f_{8c}:f_{16h}:f_{8e} = 1:2:1$. In fact, in Li-doped samples the experimentally obtained relative populations of the two octahedral sites ($8(c)$ and $16(h)$) were close to the predicted values and remained almost constant up to 573 K. Different behavior was found for the fraction of probes at the tetrahedral site $8(e)$. The measured temperature variation of fraction f_{8e} for different Li contents is shown in Fig. 7. The theoretical crystallographic value of $f_{8e} = 25\%$ was observed only in $Li_{0.02}In_2S_3$ at 293 K. With increasing temperature and lithium concentration, the measured fraction of the tetrahedral $8(e)$ site decreases.

As a last point we will present the temperature dependence of the fitted quadrupole frequencies which are a measure of the strength of the EFGs. In most PAC-experiments, these frequencies are easy to

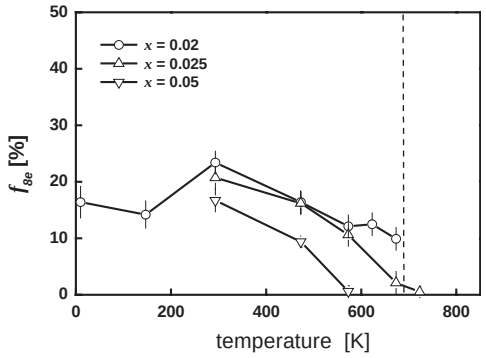

Fig. 7. The temperature dependence of the fraction f_{8e} (tetrahedral site) for different Li contents x.

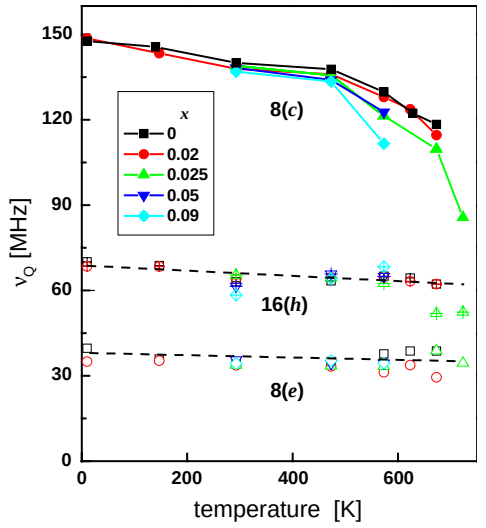

Fig. 8. Temperature dependence of the quadrupole coupling constants ν_{Qi} corresponding to the three substitutional ^{111}In sites in $Li_xIn_2S_3$.

determine because they mainly reflect the periodicity of the pattern. Fig. 8 gives an overview of all three sites at all temperatures and Li concentrations. The squares represent the data for undoped β-In_2S_3 samples [20]. Obviously, the $\nu_Q(8c)$-values strongly decrease with temperature, different to the other two sites, which show only a small decrease. Furthermore, the EFG of site $8(c)$ decreases more strongly for higher Li contents. One might object that the analysis of the smaller PAC frequencies is difficult as can be seen from Fig. 2. The usual procedure to fix some values during fitting cannot be applied in the present case, where all frequencies and fractions have to be assumed as non-constant. Therefore, in the following we will concentrate on the obvious variations of ν_Q at the site $8(c)$. Fig. 9, which is a zoom of Fig. 8, shows in more detail the temperature dependence of $\nu_Q(8c)$ from room temperature up to the $\beta \rightarrow \alpha$ phase transition temperature. At room temperature the frequency values $\nu_Q(8c)$ for samples with different Li concentrations are still close to each other—however, they decrease systematically for in-

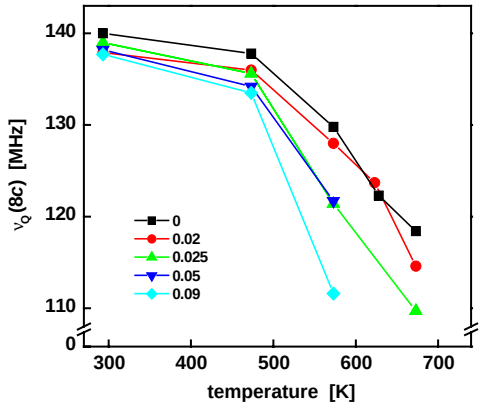

Fig. 9. The temperature dependence of $\nu_Q(8c)$—a zoom of Fig. 8 with a suppressed point zero.

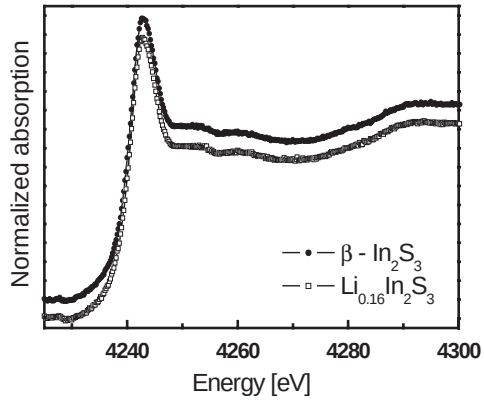

Fig. 10. XANES results obtained for the L_I absorption edge of indium.

creasing Li content and temperature. This effect is most evident at $T_m = 670$ K.

3.3. XANES measurements

The method of X-ray absorption near the edge spectroscopy (XANES) allows a characterization of the lowest empty states in the conduction band of a compound. XANES spectra may give information about the charge state of the atom and the symmetry of the direct neighborhood. In In_2S_3 two possible absorption edges have been used for the measurements. Fig. 10 shows the L_I edge of In, which corresponds to $2s \rightarrow np$ transitions. According to previous results obtained by tight-binding calculations [27], the peak at 4243 eV in the XANES spectrum can be attributed to In5p-S3p states in the conduction band. In Fig. 10 two different spectra are plotted, one for pure In_2S_3 and the other one for $Li_{0.16}In_2S_3$, which corresponds quite well with the PAC sample with the highest Li content. The two spectra are shifted vertically to demonstrate their near-identity.

However, the XANES result is different at the K-edge of sulfur (see Fig. 11), corresponding to $1s \rightarrow np$

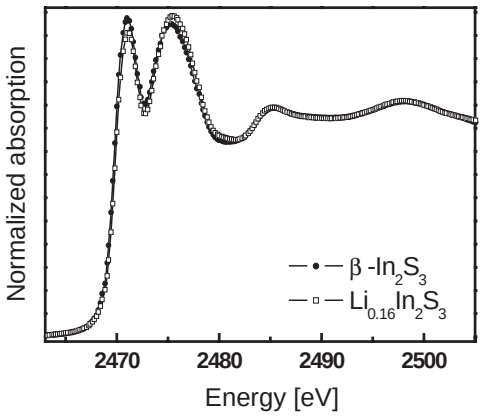

Fig. 11. XANES results obtained for the K absorption edge of sulfur.

transitions. The first peak at 2471 eV can be attributed to S3p − In5s states and the second one at 2475 eV to S3p − In5p states in the conduction band [27]. In Fig. 11 the Li-insertion results in different spectra. Li doping decreases the first peak, whereas the second one is enhanced with respect to the undoped material. This gives a direct hint that the electronic structure of the sulfur atoms has changed by the Li insertion.

4. Discussion

4.1. Mobile atoms in Li-doped samples

As already mentioned in Section 2.2, the presence of a dynamic fraction in a PAC spectrum indicates that changes have occurred in the electronic environment of the probe during the PAC observation time. We now have to understand what kind of dynamic process(es) might occur(s) in Li-doped In_2S_3. As the clue for understanding, we take the fact, that in the α-phase of *undoped* In_2S_3 *all* probes experience a dynamic HFI. As we know from the crystallographic data, a redistribution of the empty tetrahedra takes place, i.e., many In atoms have to leave their sites. During their jumps they most probably use the structurally empty octahedral sites of the spinel structure. Moreover, to observe a dynamic HFI for *all* probe atoms in the α-phase it is *not* necessary that the ^{111}In atoms themselves are in motion during their EC and subsequent γ-decay. It is sufficient, that jumps in the nearest neighborhood occur, which change the acting EFG. As proven in more detail in [21], the dynamic process in the α-phase of *pure* In_2S_3 can be explained by a diffusion of indium atoms.

The temperature dependence of the dynamic fraction f_d in $Li_xIn_2S_3$ samples with different x-values (see Fig. 5) has two features which should be explained. At temperatures above 500 K, fraction f_d slowly increases (up to 60% for $Li_{0.05}In_2S_3$). Adopting the interpretation found for the α-phase, we assume a growing mobility of the indium ions without a distinct phase transformation of the matrix, triggered by the inserted Li atoms. Furthermore, Fig. 7 gives a direct hint that In atoms leave their tetrahedral sites: fraction f_{8e} decreases in the same temperature range where f_d increases. The decrease of f_{8e} is faster for higher Li content. On the other hand, the fractions of the octahedral sites (f_{8c} and f_{16h}) stay close to the predicted values and remain almost constant up to 573 K (see Table 1).

Table 1
The fitted fractions of the three substitutional sites and the dynamic fraction in $Li_xIn_2S_3$ are given for different Li concentrations x at the measuring temperatures $T_m = 473$ and 573 K. The ratio of the octahedral sites remains about constant, the tetrahedral fraction decreases and the dynamic fraction increases

Li content x (Li/mol)	f_{8c}/f_{16h}		f_{8e} (%)		f_d (%)	
	473 K	573 K	473 K	573 K	473 K	573 K
0	0.4	0.3	21.6	21.9	0	0
0.02	0.5(1)	0.4(1)	24(2)	12(2)	20(1)	21(2)
0.025	0.4(1)	0.4(1)	16(3)	11(1)	29(2)	34(2)
0.05	0.5(1)	0.3(1)	9(2)	0.6(4)	47(2)	48(2)

As a second important result, in Fig. 6 the dynamic fraction f_d is plotted versus the Li concentration for $T_m = 293$, 473 and 573 K. All these data follow a single curve, which shows a linear correlation between f_d and the Li content for $x \leqslant 0.05$. With an increasing amount of Li, the fraction of those PAC probes observing a jumping Li in their neighborhood increases. Therefore, we propose that the observed dynamic HFI in the temperature range 250–500 K is mainly caused by fast jumping Li atoms. At temperatures above 500 K, the threshold for the In atoms on tetrahedral sites is lowered and they also start to jump away. We cannot prove that Li and In are competing for the tetrahedral site, but we would like to mention that in more complex thiospinels ($CuInSnS_4$ or $Cu_{0.5}In_{2.5}S_4$) the insertion of Li causes a rearrangement of the lattice, where Li^+ or In^{3+} cations are found on equivalent sites [11].

One sample ($x = 0.02$) was measured down to 10 K and showed a dynamic fraction of about 25% at this temperature (see Fig. 5). Following our line of interpretation this should indicate a Li motion even at 10 K. Unfortunately, only one measurement exists and some doubts may remain whether this fit to the data is necessary or not.

4.2. Changes of the ionic charge

In Fig. 9 we have demonstrated a systematic lowering of $\nu_Q(8c)$ with the measuring temperature T_m and the Li content x. In ionic compounds the strength of the EFG, or at least its scaling and symmetry, can be simply calculated by the point charge model. As the EFG is proportional to $1/d^3$ (d = distance to the next neighbor

ions), the increase of the lattice constant with increasing temperature is often the reason for a decreasing EFG. This explanation would possibly account for the slow decrease of $\nu_Q(16h)$ and $\nu_Q(8e)$ in Fig. 8, however, the dramatic decrease of $\nu_Q(8c)$ requires a different explanation. The most direct interpretation of the PAC spectrum is to assume that the regular octahedron gets larger due to the inserted Li atoms. A possible mechanism can be found from an ionic point of view. In order to obtain an electrically neutral compound after Li insertion, the *charge of the In atoms has to be reduced*, depending on the Li concentration. This can be written as the following equation:

$$In_2^{+3}S_3^{-2} + xLi^+ + xe^- \rightarrow Li_x^+ In_2^{3-x/2} S_3^{-2}. \quad (7)$$

A change of the sulfur charge can be excluded. Lithium was assumed to be a positive ion, as the disappearance of the after-effect in Li-doped In_2S_3 proves its electron-donor character. If we adopt this charge reduction of the In ions, we are able to describe the EFG dependence on the Li concentration in a very simple way.

Lowering the In charge from $q(x=0)=3$ to $q(x)=3-x/2$ reduces the binding of the next sulfur ions and, as a consequence, the distance $d(x)$ between In and S increases relative to the distance $d(x=0)=2.58$ Å in In_2S_3. The Coulomb force scales with $1/d^2$ and we get:

$$q(0)/q(x) = q/(q-x/2) = d(x)^2/d(0)^2. \quad (8)$$

Using the proportionality $\nu_Q \propto 1/d^3$, we can calculate the frequency:

$$\nu_Q(x)/\nu_Q(0) = d(0)^3/d(x)^3. \quad (9)$$

By combining the two equations we may calculate the scaling of the EFG with the Li content x:

$$\nu_Q(x) = \nu_Q(0) \times (1 - x/2q)^{3/2}. \quad (10)$$

In Fig. 12, the data of Fig. 9 are compared with this oversimplified model. For $T_m = 293$ K and 473 K the agreement is surprisingly good, while the data for $T_m = 573$ K require a modified slope of the theoretical curve.

There are some objections to this simple ionic point charge picture. First we assumed that the charge of *all* In atoms is reduced. Consequently one might expect all distances to grow and all three EFGs to show a similar concentration dependence. This is definitely in contrast to the measured quadrupole frequencies $\nu_Q(16\,h)$ and $\nu_Q(8e)$ (see Fig. 8).

The second objection leads to a more specific interpretation of the changes which occur due to the insertion of Li. The simple model introduced above can be used to calculate the increase in distance in the octahedron from 2.58 to 2.61 Å at the highest Li concentration $x=0.13$. Such an increase of about 1.2% should be visible in the lattice constants of the Li-doped samples, which we measured with XRD. As

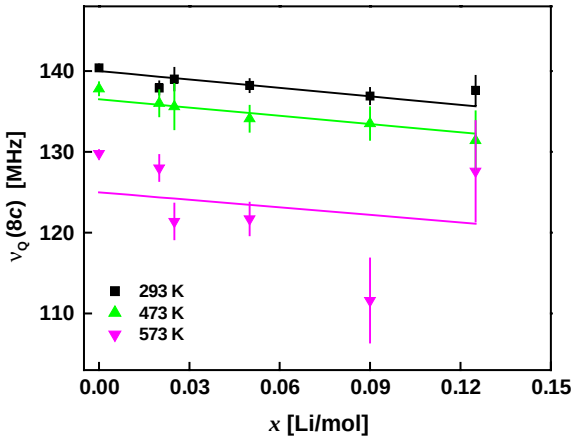

Fig. 12. $\nu_Q(8c)$ versus the Li content x for three different temperatures. The solid lines represent the calculated values according to Eq. (9).

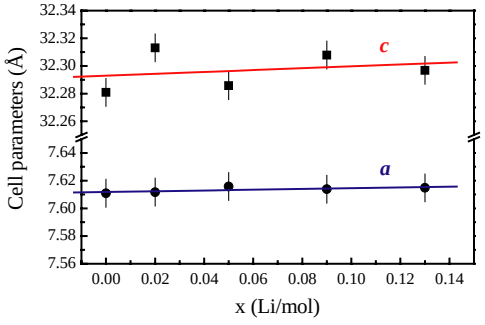

Fig. 13. The lattice constants a and c of $Li_xIn_2S_3$ measured by XRD for different Li concentrations x.

shown in Fig. 13, the increase is much smaller, i.e., the lattice constant α increases only from 7.611 to 7.615 Å, this is an increase by only 0.05%.

Although the simple model works quite well, for some of the findings we must conclude that the sulfur ions do not change their positions significantly. However, the PAC method is not sensitive to the position of the ions, but is sensitive to their charge distribution. Now we can consider the results of the XANES experiments. Here we observed no change in the indium orbitals, but changes in the sulfur orbitals. We therefore propose that the inserted Li reduces the effective charge of the In atoms, as required for the electrical neutrality of the compound. As a consequence, the molecular orbitals of the sulfur ions are modified in such a way that the center of the charge distribution is slightly shifted away from the In atom in the center. Possibly, this happens only at the regular octahedral site 8*c*.

5. Conclusions

The aim of the present study was to search for changes occurring as the consequence of Li insertion into the In_2S_3 lattice on the atomic scale of the neighbor

ions of a radioactive "spy" atom. When the PAC method is used with ^{111}In atoms these probes occupy regular In lattice sites. The experimental PAC results for pure In_2S_3 directly proved this assumption. Two different regimes of dynamical behavior are observed: at lower temperatures undoped material shows a strong damping of the PAC spectra, which is explained by the well known "EC-aftereffect" for ^{111}In probes in semiconductors. In fact, after doping In_2S_3 with the electron donor Li the higher concentration of mobile charge carriers "repairs" this damping. Of higher importance for the structural understanding of In_2S_3 is the dynamical behavior, clearly observed at the phase transition to the α-phase and above: in addition to the crystallographic information which only requires a random occupation of the empty tetrahedral sites, the PAC results give clear hints that the In atoms start to leave their tetrahedral sites at this temperature.

The picture gets more detailed after Li insertion. Although the "EC-aftereffect" has disappeared the PAC-spectra show a new dynamic behavior which increases with increasing Li content x. This dynamic damping indicates that the direct neighborhood of the probes changes within about 200 ns. We propose that for higher temperatures ($T \geqslant 500$ K) the migration of the In atoms from the tetrahedral sites starts, as can be seen from the corresponding fraction f_{8e}. This migration is favored by the presence of empty sites in the direct neighborhood of a tetrahedral site, in contrast to the octahedral sites. We therefore propose, that the Li insertion lowers the threshold which confines the In ions to the tetrahedral sites. The dynamic behavior between RT (and perhaps below) and 500 K is caused by mobile Li ions, because the dynamic fraction is proportional to the Li content x.

The final question where the Li ions might be located could not be answered. Nevertheless, a clear Li-concentration dependence was found for only one lattice site, the octahedral site 8*c*. A simple correlation with the reduced charge of the In ions seems to hold, but the addition of the XANES and XRD results indicates that what we observed was not a simple lattice expansion due to the inserted Li, but a change of the molecular orbits of the sulfur ions which shift the center of their charge distributions somewhat away from the central In ions that have a reduced effective charge. If this behavior would be restricted to site 8*c*, this might give a key for the Li localization. However, we cannot exclude that a similar Li-concentration dependence might be hidden within the error bars of the analysis of the much smaller EFGs of the other two sites in In_2S_3.

Acknowledgments

This study was supported by the Deutsche Forschungsgemeinschaft (UH 104/1-1) and the CNRS (PICS No. 505). The authors wish to thank Anne-Marie Flank and Robert Cortès for their help in collecting data of SACO and DCI experiments at LURE (Orsay, France).

References

[1] B. Scrosati, C.A. Vincent, Modern Batteries—An Introduction to Electrochemical Power Sources, Arnold, London, 1997, 198pp.
[2] M. Armand, Materials for Advanced Batteries, in: D.W. Murphy, J. Broadhead, B.C.H. Steele (Eds.), Plenum Press, New York, 1980, p. 145pp.
[3] M. Wakihara, Mater. Sci. Eng. R33 (2001) 109.
[4] M. Wachtler, M. Winter, O. Besenhard, J. Power Sources 105 (2002) 151.
[5] Y. Idota, T. Kubota, A. Matsufuji, Y. Maekawa, T. Miyasaka, Science 276 (1997) 1395.
[6] P. Poizot, S. Laruelle, S. Grugeon, L. Dupont, J.-M. Tarascon, J. Power Sources 97–98 (2001) 235.
[7] J. Yang, Y. Takeda, N. Imanishi, O. Yamamoto, Electrochim. Acta 46 (2001) 2659.
[8] C. Pérez Vicente, C. Bousquet, A. Krämer, J.L. Tirado, J. Olivier-Fourcade, J.-C. Jumas, J. Solid State Chem. 134 (1997) 238.
[9] M.L. Elidrissi Moubtassim, C. Bousquet, J. Olivier-Fourcade, J.-C. Jumas, J.L. Tirado, Chem. Mater. 10 (1998) 968.
[10] M. Cochez, P. Lavela, J. Morales, J. Olivier-Fourcade, J.-C. Jumas, J. Power Sources 62 (1996) 101.
[11] R. Dedryvère, J. Olivier-Fourcade, J.-C. Jumas, S. Denis, P. Lavela, J.L. Tirado, Electrochim. Acta 46 (2000) 127.
[12] K. Kambas, J. Spyridelis, M. Balkanski, Phys. Stat. Sol. B 105 (1981) 291.
[13] R. Diehl, R. Nitsche, J. Cryst. Growth 42 (1975) 306.
[14] J. Rodriguez Carvajal, FULLPROF: A Program for Rietveld Refinement and Pattern Matching Analysis, Abstracts of the Satellite Meeting on Powder Diffraction of the XV Congress of the IUCr, Toulouse, France, 1990, p.127.
[15] M. Uhrmacher, K. Pampus, F.J. Bergmeister, D. Purschke, K.P. Lieb, Nucl. Instrum. Methods B 9 (1985) 234.
[16] M. Uhrmacher, M. Neubauer, W. Bolse, L. Ziegeler, K.P. Lieb, Nucl. Instrum. Methods B 139 (1998) 306.
[17] H. Frauenfelder, R.M. Steffen, in: Alpha-Beta-and Gamma-Ray-Spectroscopy, Vol. 2, North-Holland, Amsterdam, 1965.
[18] G. Schatz, A. Weidinger, Nuclear Condensed Matter Physics, Wiley, West Sussex, England, 1996.
[19] J. Kajfosz, Report No: 848/Pm, Institute of Nuclear Physics, Krakow, Poland, 1973.
[20] L. Aldon, M. Uhrmacher, C. Branci, L. Ziegeler, J. Roth, P. Schaaf, H. Metzner, J. Olivier-Fourcade, J.-C. Jumas, Phys. Rev. B 58 (1998) 11303.
[21] M. Uhrmacher, L. Aldon, P. Schaaf, H. Metzner, J. Olivier-Fourcade, J.-C. Jumas, Hyperfine Interactions 120/121 (1999) 371.
[22] D. Lupascu, S. Habenicht, K.P. Lieb, M. Uhrmacher, Th. Wenzel, Phys. Rev. B 54 (1996) 871.
[23] S. Habenicht, D. Lupascu, M. Uhrmacher, L. Ziegeler, K.P. Lieb, ISOLDE Collaboration, Z. Phys. B 101 (1996) 187.
[24] L.A. Errico, M. Rentería, A.G. Bibiloni, F.G. Requejo, Hyperfine Interactions 120/121 (1999) 457.
[25] S. Habenicht, D. Lupascu, M. Neubauer, M. Uhrmacher, K.P. Lieb, ISOLDE Collaboration, Hyperfine Interaction 120/121 (1999) 445.
[26] R. Dedryvére, M. Uhrmacher, A. Lohstroh, A. Picard-García, J. Olivier-Fourcade, J.-C. Jumas, Hyperfine Interactions 136/137 (2001) 479.
[27] I. Lefebvre, M. Lannoo, J. Olivier-Foucade, J.-C. Jumas, Phys. Rev. B44 (1991) 1004.